ORIGINAL ARTICLE

A high-order accurate AUSM$^+$-up approach for simulations of compressible multiphase flows with linear viscoelasticity

M. Rodriguez[1] · E. Johnsen[1] · K. G. Powell[2]

Abstract

An Eulerian approach for simulations of wave propagation in multiphase, viscoelastic media is developed in the context of the Advection Upstream Splitting Method (AUSM). We extend the AUSM scheme to the five-equation model for simulations of interfaces between gases, liquids, and solids with constitutive relations appropriately transported. In this framework, the solid's deformations are assumed to be infinitesimally small such that they can be modeled using linear viscoelastic models, e.g., generalized Zener. The Eulerian framework addresses the challenge of calculating strains, more naturally expressed in a Lagrangian framework, by using a hypoelastic model that takes an objective Lie derivative of the constitutive relation to transform strains into velocity gradients. Our approach introduces elastic stresses in the convective fluxes that are treated by generalizing AUSM flux-vector splitting (FVS) to account for the Cauchy stress tensor. We determine an appropriate discretization of non-conservative equations that appear in the five-equation multiphase model with AUSM schemes to prevent spurious oscillations at material interfaces. The framework's spatial scheme is solution adaptive with a discontinuity sensor discriminating between smooth and discontinuous regions. The smooth regions are computed using explicit high-order central differences. At discontinuous regions (i.e., shocks, material interfaces, and contact surfaces), the convective fluxes are treated using a high-order Weighted Essentially Non-Oscillatory (WENO) scheme with AUSM$^+$-up for upwinding. The framework is used to simulate one-dimensional (1D) and two-dimensional (2D) problems that demonstrate the ability to maintain equilibrium interfacial conditions and solve challenging multi-dimensional and multi-material problems.

Keywords Five-equation model · AUSM$^+$-up · Multi-component · Linear viscoelasticity · Zener model

List of symbols

AUSM	Advection Upstream Splitting Method
FVS	Flux-vector splitting
WENO	Weighted Essentially Non-Oscillatory
FDS	Flux-difference splitting
ρ	Density
$\alpha^{(k)}$	kth component volume fraction
K	Number of materials
u_i	Velocity vector
p	Pressure
E	Total energy
σ_{ij}	Cauchy stress tensor
Q_k	Heat flux
κ	Thermal conductivity
N_r	Number of relaxation frequencies
e	Internal energy
$e^{(\mathrm{e})}$	Elastic energy
T	Temperature
NASG	Noble-Abel Stiffened-Gas
EOS	Equation of state
n, B, b, c, q	NASG EOS material properties
$\dot{\epsilon}_{ij}$	Strain-rate tensor
$\dot{\epsilon}_{ij}^{(\mathrm{d})}$	Deviatoric component of $\dot{\epsilon}_{ij}$
$\tau_{ij}^{(\mathrm{d})}$	Deviatoric component of σ_{ij}
$\tau_{ij}^{(\mathrm{v})}, \tau_{ij}^{(\mathrm{e})}$	Viscous and elastic contribution of τ_{ij}
$\mu_\mathrm{b}, \mu_\mathrm{s}$	Bulk and shear viscosities
λ_r	Relaxation time
G	Underrelaxed shear modulus
G_r	Relaxed shear modulus

✉ M. Rodriguez
mrdz@umich.edu

1 Mechanical Engineering Department, University of Michigan, Ann Arbor, MI 48109, USA

2 Aerospace Engineering Department, University of Michigan, Ann Arbor, MI 48109, USA

$H(t)$	Heaviside function
ψ	Shear relaxation function
$\varsigma^{(l)}$	lth relaxation shear coefficient
$\theta^{(l)}$	lth relaxation frequency
$\xi^{(l)}$	lth memory variable
$a^{(k)}$	kth component speed of sound
$\zeta_{\max}$	Maximum wavespeed
ν	Courant number
ν_μ, ν_κ	von Neumann numbers
$F_{i\pm 1/2}$	Interface flux
ϕ, φ	Normal and tangent convective flux
η_{kk}	Normal Cauchy stress tensor flux
η_{kl}	Tangent Cauchy stress tensor flux
$u_{k,i+1/2}$	Normal interface velocity
$u_{l,i+1/2}$	Tangent interface velocity
M, N	Normal and tangent Mach number
$\mathcal{M}$	Split Mach number function
$\mathcal{P}$	Split pressure function
$\kappa_{\mathrm{p}}, \kappa_{\mathrm{u}}$	AUSM$^+$-up coefficients
$\mathcal{A}$	AUSM discretization operator
TRR	Twin regular reflection–refraction
σ_{von}	von Mises stress

1 Introduction

The increased sophistication of numerical techniques for compressible multiphase flows has enabled studies of implosions, explosions, and ballistics, and with them the growing need to accurately resolve features with high-frequency contents (e.g., shock waves) propagating into heterogeneous media. These flows involve regions of low Mach numbers in homogeneous solids or liquids, while Mach numbers can be supersonic in gas/liquid mixture regions where the sound speed can be as low as tens of meters per second. Shocks emitted from implosions propagate into surrounding media, causing permanent deformations and possibly material loss. An example of interest is cavitating bubble clouds collapsing over a hydrofoil's surface [1–3]. Computing such flows requires high-order accuracy to resolve broadband motions, robustness to be applicable across a range of Mach numbers (including nearly incompressible flow), and computational efficiency to represent a wide range of scales (e.g., bubble clouds, cavitation sheets, turbulence). Flux-difference splitting (FDS) or flux-vector splitting (FVS) are common approaches to address these issues. FDS schemes are popular given their relatively simple implementation. However, representation of flows across a wide range of Mach numbers is not straightforward. On the other hand, FVS schemes, in particular the AUSM schemes first developed by Liou and Steffen [4], are capable of computing all-speed flows [5,6] and multiphase flows [7–12].

AUSM schemes have been used to study multiphase shock wave propagation and shock-droplet problems involving gases and liquids [11]. Here, the motivation is to develop a coupled fluid–solid approach to study problems such as cavitation bubbles collapsing near solid surfaces. The extension of an Eulerian framework to represent deformations, more adequately expressed in a Lagrangian framework, is non-trivial. Two major approaches have been pursued in the literature [13]: Godunov-based (hyperelastic models) and conventional (hypoelastic models). The former accounts for finite deformations and ensures thermodynamic consistency in an Eulerian framework. This approach has been used in conjunction with FDS schemes to study ballistics [14,15], and implosions [16] with interface-tracking approaches and ballistics with interface-capturing approaches [17]. However, it is not clear how to implement FVS schemes with the Godunov approach, specifically, the fluxes involving the deformation tensor. Leveraging our previous work [18], we follow the hypoelastic approach as it is possible to formulate an Eulerian framework for simple linear viscoelastic models for materials under the small-strain assumption. This limitation is acceptable for problems with small deformations, e.g., for materials with large Young's modulus relative to the pressure loads. An objective Lie temporal derivative of the elastic contribution of the Cauchy stress tensor is taken, thus transforming Lagrangian strains in the constitutive relation into velocity gradients [19]. As a result, the convective fluxes are modified by additional elastic components, such that the implementation of FVS schemes, as developed for the Euler equations where the Cauchy stress tensor involves only pressure, is not trivial. We address this issue here for the AUSM scheme by generalizing flux vectors to Cauchy stress tensors describing linear viscoelastic constitutive relations.

The representation of material interfaces typically falls under one of two approaches: tracking or capturing. The former, while being able to resolve the interface exactly, involves solving non-conservative equations that may lead to conservation issues. AUSM schemes have been used in interface-tracking approaches, e.g., the Ghost Fluid Method, in conjunction with arbitrary Lagrangian–Eulerian frameworks [20,21]. While conservation issues can be mitigated, the overall solver can become complicated and involves two different solvers, one for the flow and one for the solid dynamics, to be appropriately coupled. Moreover, comparisons of AUSM schemes and FDS schemes demonstrated AUSM schemes to be numerically stiffer in such problems [20]. In the latter approach, the interface is regularized over a few cells in a fashion that ensures conservation using a single-solver framework. Although the six-equation multiphase model has been used with AUSM schemes [11], the five-equation model is appealing for the simplicity of its implementation and because it does not require the calculation of the complicated source terms present in the six-equation

model. The five-equation multiphase model has been implemented successfully for FDS schemes that eliminate spurious errors due to the inconsistent treatment of primitive variables and maintain equilibrium conditions [22]. There have been efforts toward high-order accurate numerical approaches using FVS schemes for multiphase compressible flows that prevent spurious errors [23]; however, this approach only considers gases described by the ideal gas law. The five-equation model has yet to be extended to FVS-type schemes for multi-component flows.

By following the analysis of [24,25] and using the AUSM$^+$-up scheme, we obtain the appropriate discretization for the non-conservative equations in the five-equation model, which prevent spurious errors at material interfaces. In an extensive study of AUSM schemes with high-order approaches, Scandaliato and Liou [26] suggest utilizing characteristic variable reconstruction WENO with AUSM schemes to avoid the oscillations present in other reconstructions that would lead to a stiff scheme; we utilize primitive variable reconstruction WENO scheme of [25] due to its straightforward implementation and ability to eliminate spurious errors. Our objective is to extend AUSM schemes to interface-capturing approaches for gas–liquid–solid flows in which the solid behaves in a linear viscoelastic fashion. Furthermore, we focus on high-order-accurate spatial discretizations that result in a single, solution-adaptive framework to compute compressible multiphase flows with viscoelasticity. The paper is organized as follows. The physical model is first presented, followed by a description of the numerical model. Thereafter, the AUSM implementation for interface capturing and viscoelastic media is outlined. The approach is then tested using a series of one- and two-dimensional problems. Finally, the work is summarized, and future directions are outlined.

2 Physical model

2.1 Equations of motion

The equations governing the phenomena of interest are mass conservation, momentum, and energy balance:

$$\frac{\partial \rho}{\partial t} + \frac{\partial}{\partial x_j}(\rho u_j) = 0, \tag{1a}$$

$$\frac{\partial}{\partial t}(\rho u_i) + \frac{\partial}{\partial x_j}(\rho u_i u_j - \sigma_{ij}) = 0, \tag{1b}$$

$$\frac{\partial E}{\partial t} + \frac{\partial}{\partial x_j}(E u_j - \sigma_{ij} u_i) = -\frac{\partial Q_k}{\partial x_k}, \tag{1c}$$

$$\frac{\partial}{\partial t}(\rho^{(k)} \alpha^{(k)}) + \frac{\partial}{\partial x_j}(\rho^{(k)} \alpha^{(k)} u_j) = 0, \tag{1d}$$

where ρ is the total density, u_i the velocity vector, σ_{ij} the Cauchy stress tensor, Q_k the heat flux, $\alpha^{(k)}$ the volume fraction of material k, $k = 1, \ldots, K - 1$, K the total number of materials, and indices i, $j = 1, 2$, and 3. Equation (1d) is a mass conservation equation for $K - 1$ materials. Material k has volume fraction $\alpha^{(k)}$ and density $\rho^{(k)}$, with the following relations

$$\sum_k \rho^{(k)} \alpha^{(k)} = \rho, \qquad \sum_k \alpha^{(k)} = 1. \tag{2}$$

As described in Sect. 3.2, $K - 1$ additional mass balance equations along with the total density balance equation, corresponding to the K materials, must be evolved. The total energy per unit volume, E, is comprised of the internal, kinetic, and elastic contributions:

$$E = \rho e + \frac{1}{2}\rho u_i^2 + \rho e^{(e)}. \tag{3}$$

The internal energy (per unit volume) ρe is determined through the equation of state described in the next section, and the elastic energy $\rho e^{(e)}$ is described in Sect. 2.3.

2.2 Equation of state

The Noble-Abel Stiffened-Gas (NASG) equation of state (EOS) [27] is used to relate the internal energy to pressure and temperature in gases, liquids, and solids:

$$\rho e = \frac{p(1 - \rho b)}{n - 1} + \frac{n B(1 - \rho b)}{n - 1} + \rho q \tag{4a}$$

$$= \rho c T + B(1 - \rho b) + \rho q, \tag{4b}$$

where T is the temperature and q, n, B, b, and c are material properties empirically for liquids and solids [27–29]. The equation reduces to the stiffened-gas equation of state [29] with $b = 0$ and modifying the other material properties appropriately. In the limit of ideal gases, $B = 0, b = 0$, $q = 0$, c is the specific heat at constant volume and $n = \gamma$ is the ratio of specific heats. Table 1 provides the values of the material properties used in this work.

Table 1 Material properties corresponding to different media described by the Noble-Abel Stiffened-Gas equation of state

Property	Air	Water and model Zener solid
n	1.4	1.19
b (m^3/kg $\times 10^{-4}$)	0	6.61
B (Pa $\times 10^6$)	0	702.8
q (kJ/kg)	0	-1.167
c (kJ/kg K)	0.718	4.167

2.3 Constitutive relations

Constitutive relations for the heat flux and Cauchy stress tensor are required. For the former, Fourier conduction describes the heat diffusion process:

$$Q_k = -\kappa \frac{\partial T}{\partial x_k}, \tag{5}$$

where κ is the thermal conductivity.

For the latter, we first define the strain-rate tensor and its deviatoric component

$$\dot{\epsilon}_{ij} = \frac{1}{2}\left(\frac{\partial u_i}{\partial x_j} + \frac{\partial u_j}{\partial x_i}\right), \qquad \dot{\epsilon}_{ij}^{(d)} = \dot{\epsilon}_{ij} - \frac{1}{3}\dot{\epsilon}_{kk}\delta_{ij}, \tag{6}$$

where the dot denotes the Lie objective temporal derivative. The Cauchy stress tensor can be written in terms of isotropic (bulk) and deviatoric contributions

$$\sigma_{ij} = -p\delta_{ij} + \mu_b\dot{\epsilon}_{kk}\delta_{ij} + \tau_{ij}^{(d)}, \tag{7}$$

where the first two terms are the mechanical pressure and bulk (dilatational) viscous isotropic contributions, the third term the deviatoric stress, and μ_b the bulk viscosity. We consider the Zener constitutive model suitable for materials exhibiting elasticity, viscosity, and stress relaxation. We consider elasticity in the infinitesimally small-strain limit such that the stress and its rate depend linearly on the strain and its rate [30]:

$$\lambda_r\dot{\tau}_{ij}^{(d)} + \tau_{ij}^{(d)} = 2\mu_s\dot{\epsilon}_{ij}^{(d)} + 2G\epsilon_{ij}^{(d)}, \tag{8}$$

where the viscous contribution is $\tau_{ij}^{(v)} = 2\mu_s\dot{\epsilon}_{ij}^{(d)}$, the elastic contribution $\tau_{ij}^{(e)} = 2G\epsilon_{ij}^{(d)}$, λ_r the relaxation time, μ_s the shear viscosity, and G the shear modulus. The elastic energy is defined as

$$\rho e^{(e)} = \frac{\tau_{ij}^{(e)}\tau_{ij}^{(e)}}{4G}. \tag{9}$$

Moreover, the Zener model has the advantage of reducing to other simple linear constitutive relations [31–33]. We can generalize the Zener model to account for multiple relaxation frequencies. To do so, a shear relaxation function is defined as [31]

$$\psi = G_r\left(1 + \sum_{l=1}^{N_r} \varsigma^{(l)}\exp(-\theta^{(l)}t)\right)H(t), \tag{10}$$

where G_r is the relaxed shear modulus, $\varsigma^{(l)}$ the relaxation shear coefficient corresponding to relaxation frequency $\theta^{(l)}$, N_r the total number of relaxation frequencies, and $H(t)$ the Heaviside function. The elastic stress is a convolution of the shear relaxation function and (deviatoric) strain rate

$$\tau_{ij}^{(d)} = 2\psi(t) * \epsilon_{ij}^{(d)}. \tag{11}$$

Taking an objective Lie temporal derivative and introducing evolution equations of the memory variables close the system.

3 Numerical model

3.1 Zener model in an Eulerian framework

The main challenge with incorporating elasticity into a shock-capturing framework lies in the representation of deformations or strains. An objective temporal derivative of the elastic contribution of the deviatoric stress is taken to transform strains into strain rates. The Lie derivative is used to make this transformation [18,34]

$$\dot{\tau}_{ij}^{(e)} = \frac{\partial \tau_{ij}^{(e)}}{\partial t} + u_k\frac{\partial \tau_{ij}^{(e)}}{\partial x_k} - \tau_{kj}^{(e)}\frac{\partial u_i}{\partial x_k} - \tau_{ik}^{(e)}\frac{\partial u_j}{\partial x_k} + \tau_{ij}^{(e)}\frac{\partial u_k}{\partial x_k}, \tag{12}$$

where the first two terms are the material derivative of the stress tensor and the rest of the terms contribute to preserving objectivity. Here, we incorporate the material derivative and (1a) into the Lie derivative to transport elastic stress tensor and memory variable discontinuities, which yields [18]

$$\frac{\partial}{\partial t}\left(\rho\tau_{ij}^{(e)}\right) + \frac{\partial}{\partial x_j}\left(\rho\tau_{ij}^{(e)}u_j\right) = \rho\left[2G\dot{\epsilon}_{ij}^{(d)} + \sum_{l}^{N_r}\xi_{ij}^{(l)}\right]$$
$$+ \rho\left[\tau_{kj}^{(e)}\frac{\partial u_i}{\partial x_k} + \tau_{ik}^{(e)}\frac{\partial u_j}{\partial x_k} - \tau_{ij}^{(e)}\frac{\partial u_k}{\partial x_k}\right], \tag{13a}$$

$$\frac{\partial}{\partial t}\left(\rho\xi_{ij}^{(l)}\right) + \frac{\partial}{\partial x_j}\left(\rho\xi_{ij}^{(l)}u_j\right)$$
$$= \rho\left[\xi_{kj}^{(l)}\frac{\partial u_i}{\partial x_k} + \xi_{ik}^{(l)}\frac{\partial u_j}{\partial x_k} - \xi_{ij}^{(l)}\frac{\partial u_k}{\partial x_k}\right]$$
$$- \rho\left[\theta^{(l)}\left(2\varsigma^{(l)}G_r\dot{\epsilon}_{ij}^{(d)} + \xi_{ij}^{(l)}\right)\right], \tag{13b}$$

where $l = 1, \ldots, N_r$, $\xi_{ij}^{(l)}$ is the lth memory variable

$$\xi_{ij}^{(l)} = -\theta^{(l)}G_r\varsigma^{(l)}\exp(-\theta^{(l)}t)H(t) * \dot{\epsilon}_{ij}^{(d)}, \tag{14}$$

N_{r} the total number of relaxation frequencies corresponding to N_{r} memory variables and evolution equations, and G_{r} the relaxed shear modulus

$$G = G_{\mathrm{r}} \left(1 + \sum_{l=1}^{N_{\mathrm{r}}} \varsigma^{(l)} \right), \tag{15}$$

where $\varsigma^{(l)}$ are the relaxation coefficients for the given material, which can be obtained by material characterization [35]. The memory variable evolution equations close the system without having to perform the temporal convolution in (14).

Using the Lie derivative, the generalized Zener model equations are (1a), (1d), (13), and the momentum and energy balance equations:

$$\frac{\partial}{\partial t}(\rho u_i) + \frac{\partial}{\partial x_j}\left(\rho u_i u_j + p\delta_{ij} - \tau_{ij}^{(\mathrm{e})}\right)$$
$$= \frac{\partial}{\partial x_j}\left(\tau_{ij}^{(\mathrm{v})} + \mu_{\mathrm{b}}\dot{\epsilon}_{kk}\delta_{ij}\right), \tag{16a}$$

$$\frac{\partial E}{\partial t} + \frac{\partial}{\partial x_j}\left[(E+p)u_j - \tau_{ij}^{(\mathrm{e})}u_i\right]$$
$$= \frac{\partial}{\partial x_j}\left[u_i\left(\tau_{ij}^{(\mathrm{v})} + \mu_{\mathrm{b}}\dot{\epsilon}_{kk}\delta_{ij}\right)\right] + \frac{\partial}{\partial x_j}\left(\kappa\frac{\partial T}{\partial x_j}\right). \tag{16b}$$

3.2 Multi-material framework

To represent different materials, we use the five-equation compressible multiphase model [22,36,37] for gases, liquids, and solids [18]. All materials are assumed to obey the same equation of state and constitutive relation, but with different properties. Numerical dissipation at interfaces gives rise to a (numerical) mixture region of $\sim$ 4–5 computational cells in which appropriate rules must be specified to prevent spurious errors. In addition to the total mass conservation equation (1a), $K - 1$ species conservation equations are solved in both conservative form as in (1d) and in non-conservative form to maintain interfacial equilibrium conditions for velocity, pressure, and temperature [22]

$$\frac{\partial \alpha^{(k)}}{\partial t} + u_j\frac{\partial \alpha^{(k)}}{\partial x_j} = \Gamma^{(k)}\frac{\partial u_j}{\partial x_j}, \tag{17}$$

where $k = 1, \ldots, K - 1$ and

$$\Gamma^{(k)} = \frac{\alpha^{(k)}}{K_{\mathrm{s}}^{(k)}}\left(\frac{1}{\sum_l \frac{\alpha^{(l)}}{K_{\mathrm{s}}^{(l)}}} - K_{\mathrm{s}}^{(k)}\right), \tag{18}$$

$$K_{\mathrm{s}}^{(k)} = \rho^{(k)}(a^{(k)})^2 = \frac{n^{(k)}(p + B^{(k)})}{(1 - \rho^{(k)}b^{(k)})}. \tag{19}$$

Although necessary to represent compressible multiphase problems with significant dilatational effects, the right-hand side of this equation is sometimes set to zero [36,38,39]. In this work, we assume dilatational effects are such that the right-hand side is negligible and thus neglect these terms. When using AUSM$^+$-up with the source terms, the system becomes considerably stiffer; future studies will investigate how to incorporate this term in this framework.

The pressure and temperature are computed based on the internal energy as follows:

$$p = \frac{E - \rho\frac{u_i^2}{2} - \rho e^{(\mathrm{e})} - \sum_k \rho^{(k)}\alpha^{(k)}q^{(k)}}{\sum_k \alpha^{(k)}\frac{1}{n^{(k)}-1}}$$
$$- \frac{\sum_k \alpha^{(k)}\frac{n^{(k)}B^{(k)}(1-\rho^{(k)}b^{(k)})}{n^{(k)}-1}}{\sum_k \alpha^{(k)}\frac{1}{n^{(k)}-1}}, \tag{20a}$$

$$T = \frac{E - \rho\frac{u_i^2}{2} - \rho e^{(\mathrm{e})} - \sum_k \rho^{(k)}\alpha^{(k)}q^{(k)}}{\sum_k \rho^{(k)}\alpha^{(k)}c^{(k)}}$$
$$- \frac{\sum_k \alpha^{(k)}(1 - \rho^{(k)}b^{(k)})B^{(k)}}{\sum_k \rho^{(k)}\alpha^{(k)}c^{(k)}}, \tag{20b}$$

where terms with $\rho^{(k)}\alpha^{(k)}$ are calculated using (1d), and terms with $\alpha^{(k)}$ only are calculated using (17), as described in [22]. The internal energy can be calculated by rearranging (20). Mixture material properties ϕ (e.g., elastic moduli, viscosities, thermal conductivity) are weighted by the volume fraction:

$$\phi = \sum_k \alpha^{(k)}\phi^{(k)}. \tag{21}$$

The spatial gradients of $\alpha^{(k)}$ are computed to obtain the spatial gradients of ϕ.

4 Numerical method

4.1 Baseline temporal and spatial schemes

We use the standard explicit fourth-order Runge–Kutta scheme for time marching. Accounting for advection and diffusion, the minimum time step is computed:

$$\Delta t = \min\left(\nu\frac{\Delta x}{\zeta_{\max}}, \nu_\mu\frac{\Delta x^2}{(\mu_{\mathrm{s}}/\rho)}, \nu_\kappa\frac{\Delta x^2}{(\kappa/\rho c)}\right), \tag{22}$$

where Δx is the mesh size, $\zeta_{\max}$ the maximum global wave speed, ν is the Courant number, and ν_μ and ν_κ are the von Neumann numbers for viscous and thermal diffusion. Unless stated otherwise, we set $\nu = 0.75$ and $\nu_\mu = \nu_\kappa = 0.125$. The maximum wave speed is calculated using the maximum eigenspeed and incorporating the effect of linear viscoelasticity [18]:

$$\zeta_{\max} = \max_j \left(|u| \pm \sqrt{\frac{n(p+B)}{\rho(1-\rho b)} + \frac{4G/3 + \tau_{jj}^{(e)}}{\rho}} \right)_j.$$

The spatial discretization is based on a solution-adaptive approach that introduces numerical dissipation only where necessary. The discontinuity sensor of [18,22,40] detects shocks, contact discontinuities, and material interfaces, such that the convective fluxes are computed as follows:

$$F_{i\pm1/2} = \begin{cases} F_{i+1/2}|_{\text{AUSM}^+\text{-up}}, & \text{if } \Phi_A > 10^{-4} \ \forall A \\ F_{i+1/2}|_{\text{central}}, & \text{otherwise,} \end{cases} \quad (23)$$

where the subscripts "central" and "AUSM$^+$-up" are explained below, and

$$\Phi_A = \frac{4\phi_A}{(1+\phi_A)^2}, \qquad \phi_A = \frac{|A_R - A_L|}{A_R + A_L}, \quad (24)$$

where A is p, ρ, or n, and L and R denote the left and right edges of a computational cell. If $\Phi_A > 10^{-4} \ \forall A$ in a given cell, the solution is considered discontinuous and the WENO approach of [25] is used for all the primitive variables along with AUSM$^+$-up [10] generalized to viscoelasticity in the context of the five-equation multiphase model. The sensor is not activated for smooth problems, i.e., central differences are used exclusively in such problems. If discontinuities are detected, shock/interface capturing is applied. Although the capturing scheme is second-order, it does not affect the overall convergence rate, since problems with discontinuities exhibit first-order convergence only. Derivatives in the diffusion and source terms and material properties are computed using explicit fourth-order central differences. The numerical method has been verified to be high-order accurate for smooth problems and at most first-order accurate at discontinuities using a FDS scheme in conjunction with the HLL Riemann solver [18].

4.2 Implementation of the AUSM$^+$-up scheme for the compressible, Zener model

AUSM schemes were extended to solve the compressible Navier–Stokes equations for multiphase flows [7,9–11]. The constitutive relation for the Cauchy stress tensor is $\sigma_{ij} = -p\delta_{ij} + \mu_b\epsilon_{kk}\delta_{ij} + \tau_{ij}^{(v)}$, for Newtonian fluids. AUSM schemes split the flux into *convective* and *pressure* flux contributions [41], with the viscous terms computed separately. We first generalize the AUSM$^+$-up flux-vector splitting to solve the numerical model with a general Cauchy stress tensor; we then extend this procedure to the generalized Zener model. For brevity, the extension of AUSM$^+$-up for all speeds is not presented, but can be obtained in a straightforward

fashion following [5]. We start by formulating the AUSM flux-vector splitting to (1) using the U-splitting form [42] for a Cauchy stress tensor described by linear viscoelasticity

$$\begin{aligned} F_{k,i+1/2} = {} & \max(u_{k,i+1/2}, 0)\varphi_L + \min(u_{k,i+1/2}, 0)\varphi_R \\ & + \max(u_{l,i+1/2}, 0)\psi_L + \min(u_{l,i+1/2}, 0)\psi_R \\ & + \eta_{i+1/2}, \end{aligned} \quad (25)$$

where $k \neq l$, the first subscript denotes the flux-vector direction, and the second the discretization index. The subscripts L and R indicate the left and right edges of the computational cell, respectively, whose values are calculated using WENO [25]. To account for the second term in the convective flux in (16b), an additional convective flux vector, ψ, is needed alongside the conventional convective flux vector in AUSM$^+$-up, and the pressure flux is generalized to the Cauchy stress tensor flux

$$\varphi = \begin{bmatrix} \rho \\ \rho u_l \\ E - \sigma_{kk} \\ \rho^{(k)}\alpha^{(k)} \end{bmatrix}, \quad \psi = \begin{bmatrix} 0 \\ 0 \\ \sigma_{kl} \\ 0 \end{bmatrix}, \quad \eta = \begin{bmatrix} 0 \\ -\sigma_{kl} \\ 0 \\ 0 \end{bmatrix}, \quad (26)$$

where $k \neq l$. The velocities $u_{k,i+1/2}$ and $u_{l,i+1/2}$ are computed using the AUSM$^+$-up Mach number splitting [10]

$$\begin{aligned} u_{k,i+1/2} = {} & a_{1/2}(\mathcal{M}_{(4)}^+(M_L) + \mathcal{M}_{(4)}^-(M_R)) \\ & + \kappa_p\max(1 - \bar{M}^2, 0)\frac{(\sigma_L - \sigma_R)}{\rho_{1/2}a_{1/2}}, \end{aligned} \quad (27a)$$

$$u_{l,i+1/2} = a_{1/2}(\mathcal{M}_{(4)}^+(N_L) + \mathcal{M}_{(4)}^-(N_R)), \quad (27b)$$

where the subscripts of $\mathcal{M}$ are the order of the polynomial used, the left and right Mach numbers

$$M_{L/R} = \frac{u_{k,L/R}}{a_{1/2}}, \quad N_{L/R} = \frac{u_{l,L/R}}{a_{1/2}},$$

the interface values arithmetic averages, with $a_{1/2} = (a_L + a_R)/2$, $\bar{M}^2 = (M_L^2 + M_R^2)/2$, and the coefficient $\kappa_p = 0.4$ unless stated otherwise. The third terms of (27) and (28), are the "up" velocity–stress coupling terms that add the necessary dissipation to handle flows with large density ratios [9,10]. The tangent velocity $u_{l,i+1/2}$ and Cauchy stress tensor flux $\eta_{kk,i+1/2}$ in (27) and (28), respectively, are attributed to the elastic shear wave. Since the shear wave is not significantly affected by the large density gradients relative to their normal stress wave counterparts, these terms are computed without the "up"-dissipation terms. The split Mach number functions are defined

$$\mathcal{M}_{(4)}^{\pm} = \begin{cases} \mathcal{M}_{(1)}^{\pm}, & \text{if} \quad |M| \geq 1, \\ \mathcal{M}_{(2)}^{\pm}\left[1 \mp 2\mathcal{M}_{(2)}^{\mp}\right], & \text{otherwise}, \end{cases}$$

$$\mathcal{M}_{(1)}^{\pm} = \frac{M \pm |M|}{2}, \quad \mathcal{M}_{(2)}^{\pm} = \pm\frac{(M \pm 1)^2}{4}.$$

The Cauchy stress tensor flux is defined using the same approach as the AUSM$^+$-up pressure flux

$$\begin{aligned} \eta_{kk,i+1/2} &= \mathcal{P}_{(5)}^+(M_L)\sigma_{kk,L} + \mathcal{P}_{(5)}^-(M_R)\sigma_{kk,R} \\ &\quad + \kappa_{\mathrm{u}}\mathcal{P}_{(5)}^+(M_L)\mathcal{P}_{(5)}^-(M_R)\rho_{1/2}a_{1/2}(u_L - u_{\mathrm{r}}), \end{aligned}$$ (28a)

$$\eta_{kl,i+1/2} = \mathcal{P}_{(5)}^+(M_L)\sigma_{kl,L} + \mathcal{P}_{(5)}^-(M_R)\sigma_{kl,R}, \tag{28b}$$

where $k \neq l$,

$$\mathcal{P}_{(5)}^{\pm} = \begin{cases} \mathcal{M}_{(1)}^{\pm}/M, & \text{if} \quad |M| \geq 1, \\ \mathcal{M}_{(2)}^{\pm}\left[\pm 2 - M \mp 3M\mathcal{M}_{(2)}^{\mp}\right], & \text{otherwise}, \end{cases}$$

$\bar{M} = (M_L + M_R)/2$, and the coefficient $\kappa_{\mathrm{u}} = 0.2$ unless stated otherwise. We follow [9,10] when specifying the AUSM$^+$ scheme's tunable parameters for multiphase problems and set $\alpha = 3/16$ and $\beta = 1/8$, see [5] for further details on these parameters. In other AUSM schemes [9–12], the κ_{u} and κ_{p} coefficients are set to unity to increase the scheme's dissipation and decrease the numerical stiffness. Additionally, when $\sigma_{kl} = -p\delta_{kl}$, the numerical method reverts to AUSM$^+$-up for the Euler equations and the additional convective flux vector, ψ, is not computed. Using this formulation, the x-direction AUSM$^+$-up flux vectors for the 2D generalized Zener numerical model are:

$$\phi = \begin{bmatrix} \rho \\ \rho u \\ \rho v \\ E - \sigma_{11} \\ \rho\alpha^{(k)} \\ \rho\tau_{ij}^{(e)} \\ \rho\xi_{ij}^{(l)} \end{bmatrix}, \quad \psi = \begin{bmatrix} 0 \\ 0 \\ 0 \\ -\tau_{12}^{(e)} \\ 0 \\ 0 \\ 0 \end{bmatrix}, \quad \eta = \begin{bmatrix} 0 \\ -\sigma_{11} \\ -\tau_{12}^{(e)} \\ 0 \\ 0 \\ 0 \\ 0 \end{bmatrix},$$

where $\sigma_{11} = -p + \tau_{11}^{(e)}$ and indices $i, j = 1$ and 2. Following appropriate simplifications, the flux vectors for the generalized Zener numerical model reduce to simpler models (e.g., Kelvin–Voigt, Maxwell, and Newtonian).

4.3 Proposed AUSM$^+$-up approach for non-conservative transport equations

The non-conservative equation for the volume fraction in the multi-material framework must be carefully discretized using AUSM$^+$-up to prevent spurious errors and maintain equilibrium conditions for initially uniform flows. Following [22,24,25], we aim to consistently solve the numerical model using AUSM$^+$-up with minimal modifications to the overall method. We begin by prescribing that interfacial conditions must be maintained for a flow initialized in equilibrium, i.e.,

$$u^{n+1} = u^n = u, \quad p^{n+1} = p^n = p, \quad T^{n+1} = T^n = T,$$

where the superscripts denote the time step. Since the source terms, elastic stresses, and memory variables depend on velocity gradients, which are zero in equilibrium, those relevant terms cancel out. Only the gradients in the volume fraction and density remain. As part of the analysis, the AUSM$^+$-up operator under equilibrium conditions is first identified to determine the necessary evolution equation for the non-conservative volume fraction equation to maintain interfacial equilibrium conditions.

Applying (25) to the mass conservation equation, (1a), and considering a simple time discretization yield the AUSM$^+$-up discretization operator $\mathcal{A}(\cdot)$ such that

$$\rho_i^{n+1} = \rho_i^n - (\Delta t/\Delta x)\mathcal{A}(\rho), \tag{29}$$

where

$$\begin{aligned} \mathcal{A}(\rho) &= \left(\max(u_i^n, 0)\rho_{i+1/2,L}^n + \min(u_i^n, 0)\rho_{i+1/2,R}^n\right) \\ &\quad - \left(\max(u_i^n, 0)\rho_{i-1/2,L}^n + \min(u_i^n, 0)\rho_{i-1/2,R}^n\right). \end{aligned}$$ (30)

Discretizing the momentum balance equation, the pressure terms cancel, thus yielding the mass conservation equation if and only if $u^{n+1} = u^n$. Applying equilibrium conditions yields

$$(\rho e)_i^{n+1} = (\rho e)_i^n - (\Delta t/\Delta x)\mathcal{A}(\rho e). \tag{31}$$

The kinetic energy contribution in the total energy produces a result similar to (1a). The elastic energy contribution to the total energy also cancels out. Applying the pressure- and temperature-wise forms of the EOS for the internal energy, i.e., (21), we obtain

$$(\mathcal{X}p + \chi)_i^{n+1} = (\mathcal{X}p + \chi)_i^n - (\Delta t/\Delta x)\mathcal{A}(\mathcal{X}p + \chi), \tag{32}$$

where

$$\mathcal{X} = \sum \frac{\alpha^{(k)}}{n^{(k)} - 1} - \sum \frac{\rho^{(k)}\alpha^{(k)}b^{(k)}}{n^{(k)} - 1},$$

$$\chi = \sum \frac{\alpha^{(k)}n^{(k)}B^{(k)}}{n^{(k)} - 1} - \sum \frac{\rho^{(k)}\alpha^{(k)}b^{(k)}n^{(k)}B^{(k)}}{n^{(k)} - 1},$$

for the pressure-wise form, and

$$(\Theta T + \theta)_i^{n+1} = (\Theta T + \theta)_i^n - \mathcal{A}(\Theta T + \theta), \tag{33}$$

where

$$\Theta = \sum_k \rho^{(k)} c^{(k)} \alpha^{(k)},$$

$$\theta = \sum_k B^{(k)} \alpha^{(k)} - \sum_k B^{(k)} \rho^{(k)} \alpha^{(k)} b^{(k)},$$

for the temperature-wise form. Equations (32) and (33) are rearranged, and two equations are obtained: Equation (1d) and one equation for α to maintain pressure and temperature equilibrium,

$$(\alpha)_i^{n+1} = (\alpha)_i^n - (\Delta t / \Delta x) \mathcal{A}(\alpha). \tag{34}$$

This is a numerical discretization of the non-conservative linear advection equation for α,

$$\frac{\partial \alpha^{(k)}}{\partial t} + u \frac{\partial \alpha^{(k)}}{\partial x} = 0. \tag{35}$$

We note that the source term in (17) would cancel out since the velocity is constant initially. Quantities $\mathcal{X}, \chi, \Theta$, and θ must be computed as described above when solving for p and T to prevent spurious errors [18,22].

5 Results

We demonstrate our proposed approach by solving 1D and 2D multi-material problems with shocks. Using 1D problems, we demonstrate the framework's ability to maintain equilibrium conditions and resolve the wave structures. We solve 2D shock–cylinder interaction problems in which the cylinder is made of, alternatively, gas, water, and a Zener solid.

5.1 Material interface advection problem

We demonstrate that the five-equation framework for the AUSM$^+$-up scheme presented in Sect. 4.3 maintains equilibrium conditions at interfaces [18,22,43–45]. We consider a 1D multi-material interface problem [18] with the Zener model for the viscoelastic medium and the material properties in Table 1. The initial conditions are

$$(\rho, u, v, p) = \begin{cases} (1, 0.5, 0.5, 1/\gamma), & \text{if } x/L \in [0.25, 0.75] \\ (1000, 0.5, 0.5, 1/\gamma), & \text{otherwise,} \end{cases} \tag{36}$$

with $\tau_{11}^{(e)} = \tau_{22}^{(e)} = \tau_{12}^{(e)} = \xi_{11}^{(1)} = \xi_{22}^{(1)} = \xi_{12}^{(1)} = 0$ and $n = 1.4$ for air. For the model viscoelastic material, $\mu_b = \mu_s = 5\,\text{mPa s}$, $G = 100\,\text{MPa}$, $G_r = 50\,\text{MPa}$, $\varsigma^{(1)} = 1$, and $\theta^{(1)} = 100\,\text{MHz}$. For air, $\kappa = 0.026\,\text{W/(K m)}$, and for the model viscoelastic material, $\kappa = 0.615\,\text{W/(K m)}$. The domain is periodic with $L = 1\,\text{mm}$, $x \in [0, 1]$, and $N = 200$. The normalized errors in x-velocity, pressure, temperature, and elastic components of the Cauchy stress tensor after the solution has traveled ten domain lengths are shown in Fig. 1. At the final time, all the errors are below 4×10^{-10}. The normalized elastic stress errors for $\tau_{11}^{(e)}$ and $\tau_{22}^{(e)}$ are localized at the right interface, i.e., $x/L = 0.75$, due to the advection speed. The time histories of the normalized x-velocity, pressure, and temperature errors are plotted in Fig. 2. Within the first two periods of the simulation, the normalized temperature errors quickly rise to 10^{-8}. The temperature profile modifies the pressure through the heat transfer term such that discrepancies in pressure grow to a similar order of magnitude. For an isothermal simulation (results not shown), the normalized pressure errors do not exhibit this rise and remain bounded below 5×10^{-10}. After five periods, both temperature and pressure errors decrease by two orders of magnitude to 10^{-10}. The x-velocity errors remain bounded below 6×10^{-11}. The y-velocity and the elastic stress errors are negligible (data not shown). We conclude that our multi-material framework utilizing AUSM$^+$-up is capable of maintaining equilibrium conditions and prevents spurious interfacial errors.

5.2 Multi-material Riemann problem

We verify the extension of the five-equation multiphase model to viscoelastic media with shocks by considering the multi-material Riemann problem in [22,36,37] with viscoelasticity [18],

$$(\rho, p, \alpha^{(1)}) = \begin{cases} (1000, 10^9, 1) & \text{if } x/L \in [0, 0.7], \\ (50, 10^5, 0) & \text{otherwise,} \end{cases} \tag{37}$$

with $u = v = 0$ and $L = 1\,\text{mm}$. The initial elastic stresses are $\tau_{11}^{(e)} = \tau_{22}^{(e)} = \tau_{12}^{(e)} = 0$. For the model viscoelastic material, $\kappa = 0.615\,\text{W/(K m)}$, and for the gas, $\kappa = 0.026\,\text{W/(K m)}$. The viscous ($\mu_b = \mu_s = 50\,\text{mPa s}$) and Kelvin–Voigt ($\mu_b = \mu_s = 50\,\text{mPa s}$ and $G = 1\,\text{GPa}$) solutions are shown at $t = 240\,\mu\text{s}$ in Figs. 3 and 4 along with their respective analytical solutions. The analytical solutions are generated using the Riemann solver of [13], in which ρG is assumed constant to obtain the analytical viscoelastic solution. The numerical results show good agreement with the analytical solution since the density and pressure ratios are large. We note that all the relevant waves are captured. A spurious over-heating spike is observed in the temperature plot at the material inter-
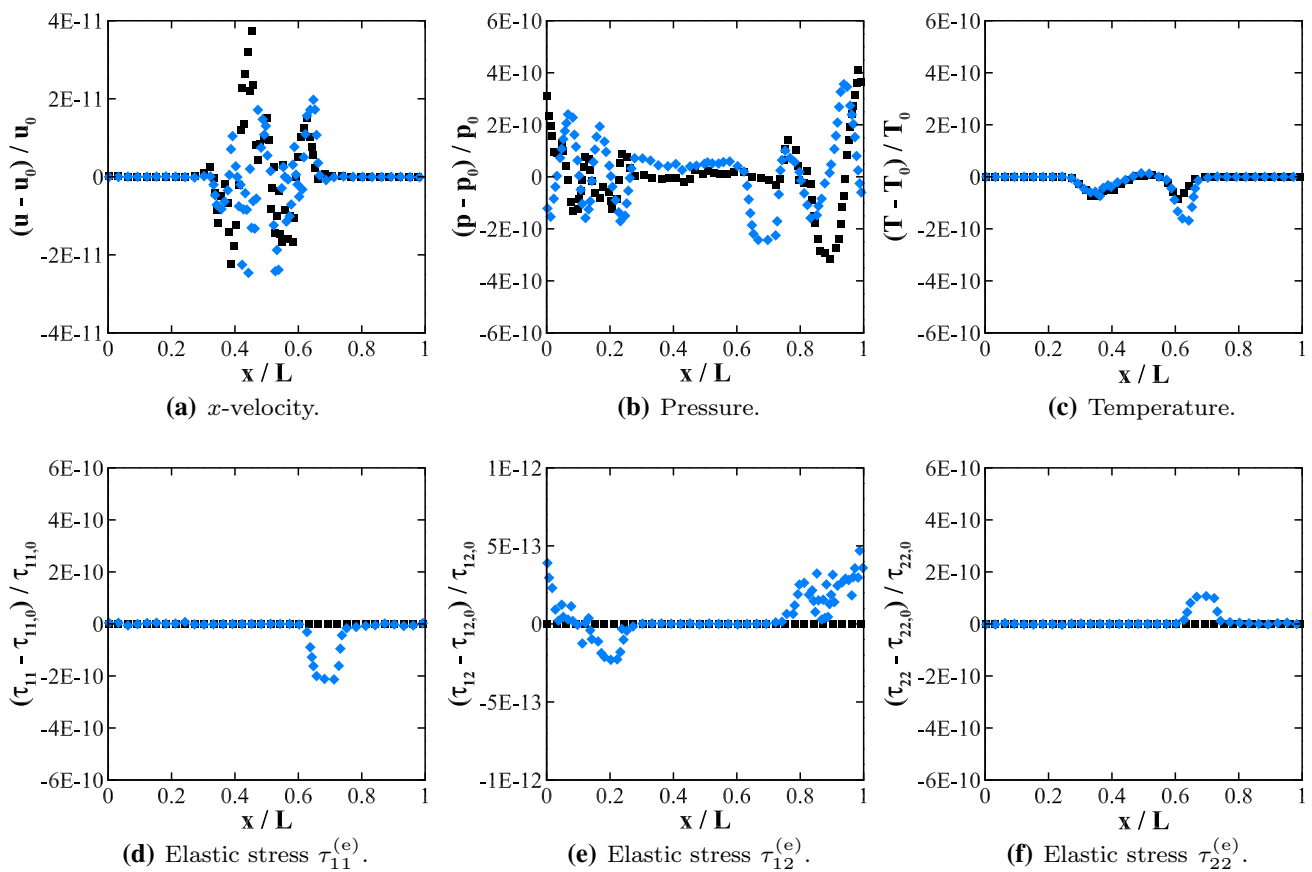
Fig. 1 Relative error in the interface advection problem after ten periods. Black squares: Newtonian liquid ($G = 0$); blue diamonds: $G = 100$ MPa
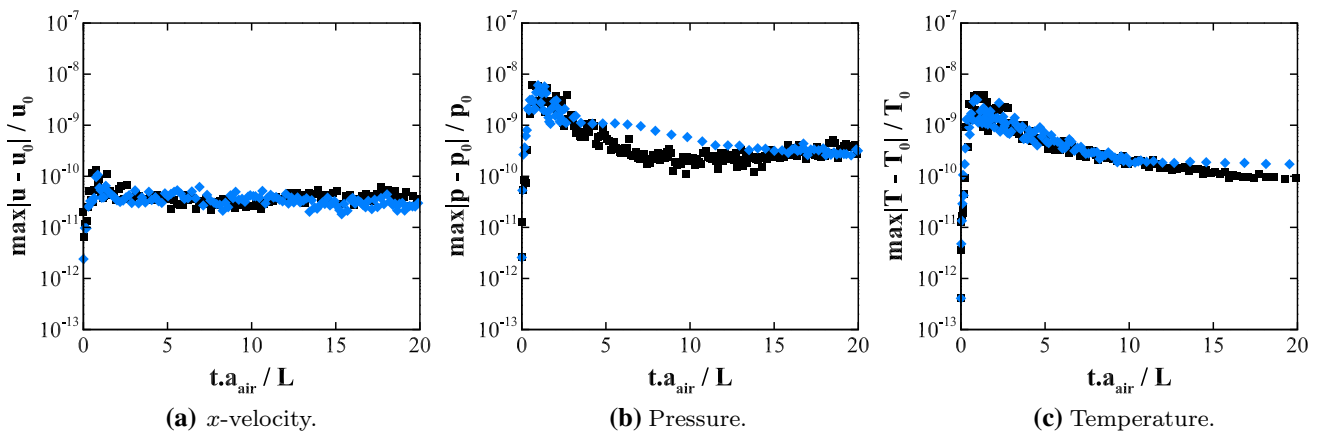

Fig. 2 Time histories of normalized L_∞ errors for the interface advection problem through ten periods. Black squares: Newtonian medium; blue diamonds: viscoelastic medium ($\mu_b = \mu_s = 5$ mPa s, $G = 100$ MPa, $G_r = 50$ MPa)

face for the Kelvin–Voigt solution. This spike has also been observed for multi-material problems and can be addressed with the fix by Fedkiw et al. [46].

5.3 2D shock–gas cylinder interaction problems

We demonstrate the numerical framework's ability to handle 2D multifluid problems by studying shock–gas cylinder interaction problems. We compute the problem studied
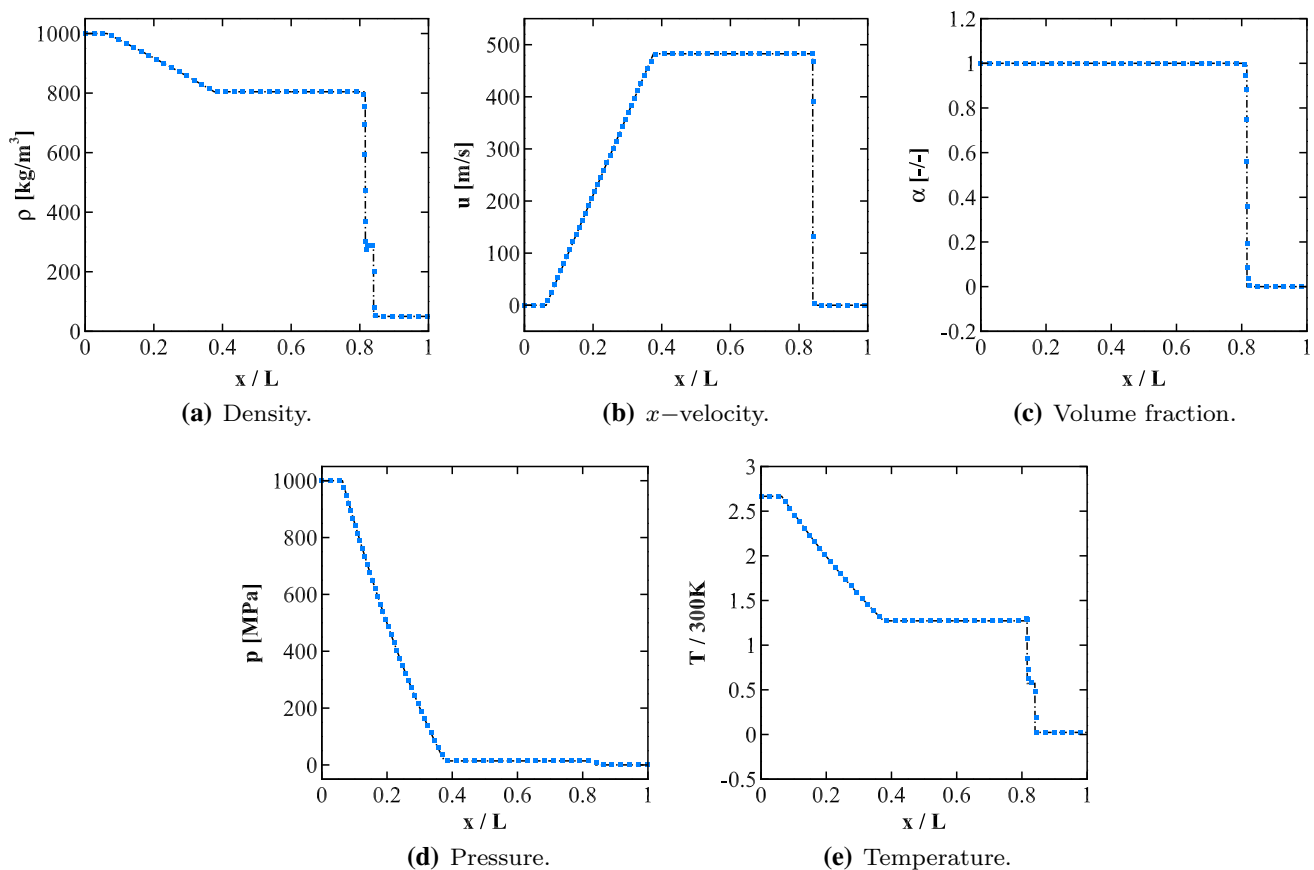
Fig. 3 Multi-material Riemann problem at $t = 240\,\mu s$ with analytical (black dashed line) and numerical (blue square) solutions for the viscous liquid–air shock wave interaction

experimentally by Haas and Sturtevant [47] and simulated numerically by Quirk and Karni [48] and others [49–51]. The initial setup is shown in Fig. 5; given the symmetry of the problem half of the domain is simulated. The initial cylinder radius is 25 mm. The computational domain extends six initial bubble radii in the x-direction from the bubble center, with $x \in [-150\,\text{mm}, 150\,\text{mm}]$ and $y \in [0\,\text{mm}, 44.5\,\text{mm}]$. The resolution is 256 points per initial cylinder radius. We define the initial cylinder radius with a diffuse interface whose volume fraction is $\alpha^{(1)} = \frac{1-\tanh(\varrho)}{2}$, where $\varrho = (R - R_o)/\Delta x$, in which $R = \sqrt{x^2 + y^2}$ and $R_o = 25\,\text{mm}$ being the initial cylinder radius. With volume fraction defined and known velocity and pressure initial conditions throughout the domain, the conservative variables ϕ are computed using the mixture relation, $\phi = \alpha^{(1)}\phi_1 + (1 - \alpha^{(1)})\phi_2$.

We solve the compressible Navier–Stokes equations for the convergent (helium) and divergent (R22) cases utilizing the same initial conditions as the experiment. The surrounding medium is air with $\rho = 1.204\,\text{kg/m}^3$ and $\kappa = 0.026\,\text{W/(K m)}$ with the remaining material properties listed in Table 1. Helium and R22 properties reported by Quirk and Karni [48] were adapted: $\rho_{\text{He}} = 0.222\,\text{kg/m}^3$,

$\kappa_{\text{He}} = 0.151\,\text{W/(K m)}$, $\rho_{\text{R22}} = 3.69\,\text{kg/m}^3$, and $\kappa_{\text{R22}} = 0.61\,\text{W/(K m)}$. The shock wave is initialized at $x = 5 \times R_0$, using the Rankine–Hugoniot conditions for a $M = 1.22$ normal shock propagating from right to left. No-penetration and no-slip boundary conditions are set along the top wall.

Select contours of the nonlinear shading function from Quirk and Karni [48] are shown for the R22 and helium cases in Figs. 6 and 8, respectively. The times shown correspond to those reported by Haas and Sturtevant [47] and shown in Figs. 7 and 9 for the R22 and helium cases, respectively. To obtain contours comparable to the experiments, the timing was set such that at time $t = 0$ the shock is at $x = 28\,\text{mm}$ from the cylinder center. Haas and Sturtevant [47] reported an error of 10% in their velocity measurements; thus, the 12% discrepancy in start time to obtain comparable contours is reasonable.

R22 gas cylinder Upon interacting with the right side of the R22 cylinder, the incoming shock is partially reflected and transmitted (frame a). Since the speed of sound in R22 is lower than that of air, the transmitted shock propagates more slowly than the shock in air (frame b). Additionally, the reflected shock wave propagates radially and is reflected
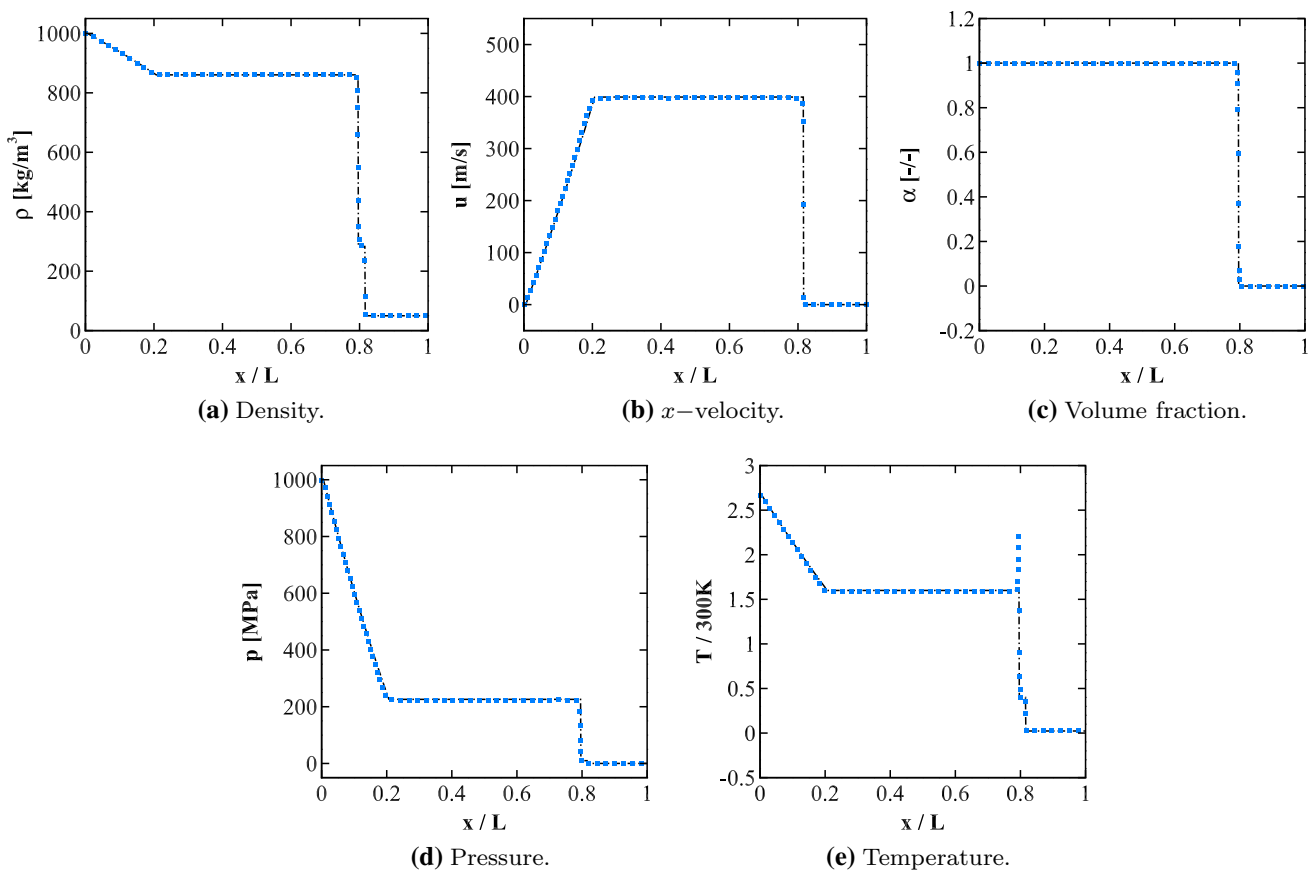
Fig. 4 Multi-material Riemann problem at $t = 240\,\mu$s with analytical (black dashed line) and numerical (blue square) solutions for the Kelvin–Voigt viscoelastic material–air shock wave interaction
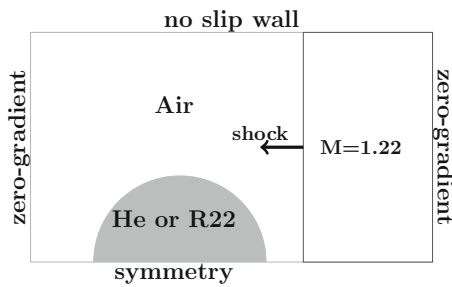

Fig. 5 Shock–gas cylinder interaction problem setup

from the top and bottom walls toward the cylinder. The incident shock intersects along the centerline after interacting with the cylinder (frame c), and the transmitted shock is partially transmitted into the air and partially reflected into the cylinder (frame d). The transmitted shock also forms a central wedge downstream of the R22–air interface comparable with the experiments. As the incident shock traverses the interface, the misalignment of density (material interface) and pressure (shock) gradients deposits baroclinic vorticity along the interface and generates roll-ups. Later, the shock is partially transmitted into the surrounding air and propagates radially

interacting with the interface; this shock is also reflected from the walls (frames d–g). The transmitted shock–interface interactions further enhance the roll-ups as the cylinder has convected to the left (frames d–g). The two-pronged feature at the downstream centerline edge of the interface noticeable in the numerical simulations of Quirk and Karni [48] is also observed. However, this feature is not as pronounced here. Moreover, fewer and smoother roll-ups develop in the later times (frame g) compared to the heavily corrugated interface in [48]. We conclude that our AUSM scheme exhibits good qualitative agreement with experiments.

Helium gas cylinder Since the impedance of the helium cylinder is lower than that of the surrounding air, the incident shock is partially transmitted as a shock and partially reflected as a rarefaction. Due to the higher speed of sound of the helium with 20% air gas ($a_{He} = 872$ m/s), the transmitted shock propagates ahead of the incident shock and reaches the downstream cylinder interface (frame a). We obtain good agreement with the flow features observed in [47,48]. At $t = 52\,\mu$s (frame b), the four-shock, twin regular reflection–refraction (TRR) configuration described in [52] is observed. The transmitted shock then reaches the downstream material
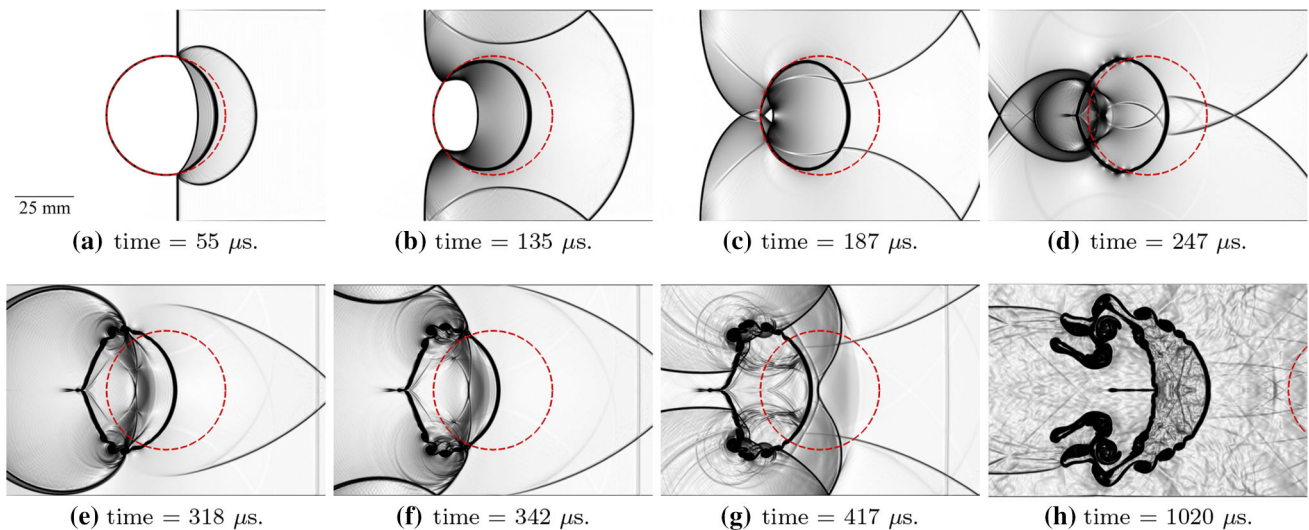
Fig. 6 Time evolution of numerical Schlieren contours for the shock–R22 gas cylinder interaction problem with a $M = 1.22$ shock moving from right to left. The red dotted outline denotes the cylinder's initial location
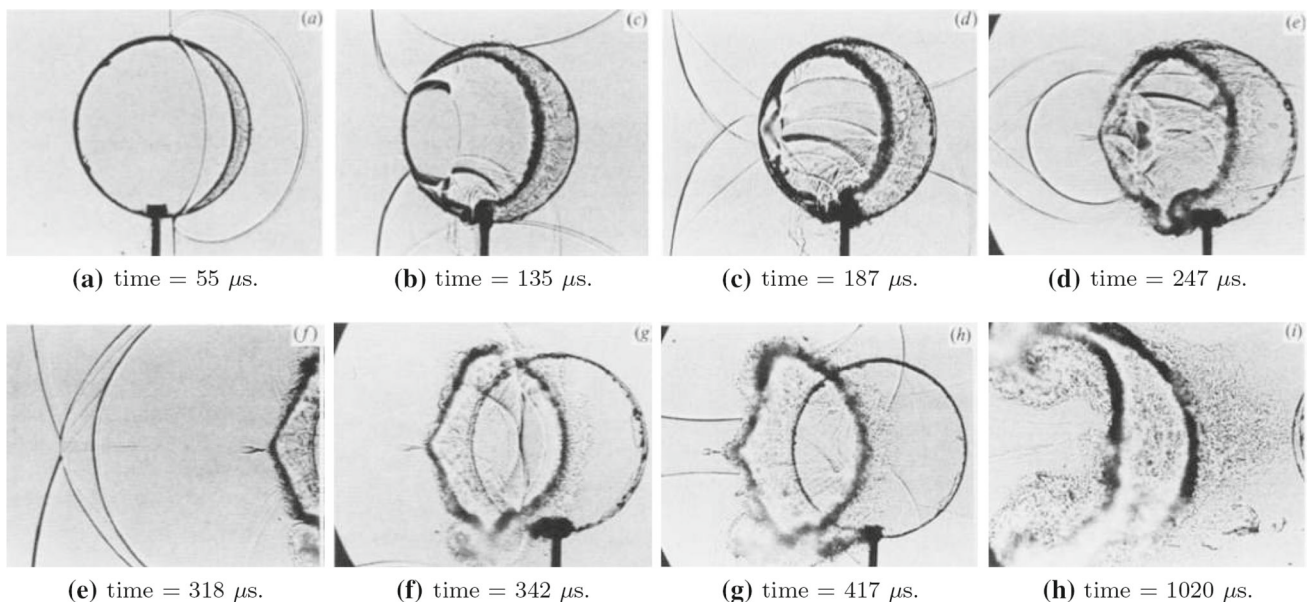

Fig. 7 Shadow photographs of the interaction of an $M = 1.22$ shock wave moving from right to left over a cylindrical R22 volume (5 cm diameter). Adapted from [47] with permission

interface at $t = 62\,\mu$s (frame c), is partially reflected, and develops into two cusps within the cylinder. These two cusps then converge, coincide, and are reflected outward to form a small hoop (frames d and e). Over time, the magnitude of the shock trapped in the cylinder decreases. Outside of the cylinder, the incident and partially transmitted shocks are reflected from the walls and the material interface (frame f). The baroclinic vorticity deposited along the material interface gives rise to a reentrant jet as the cylinder convects downstream. Unlike the simulations of [48], the roll-ups along

the interface are not observed; the cylinder's morphology in our simulations is in better agreement with the experiments. The reentrant jet develops while the cylinder takes a kidney shape as the shocks in the surroundings weaken as they leave the domain (frame g). Eventually, the upstream and downstream cylinder interfaces meet, such that the cylinder takes the form of two vortex lines symmetric upon the centerline, which convect downstream (frame h). Overall, the agreement between the proposed approach and the experiments is good.
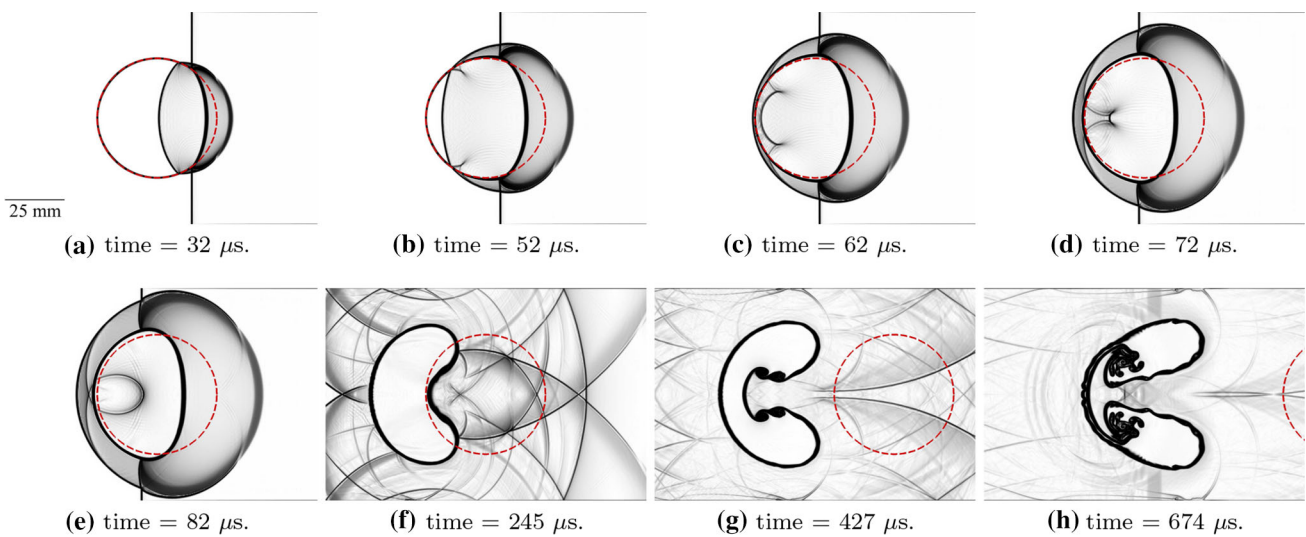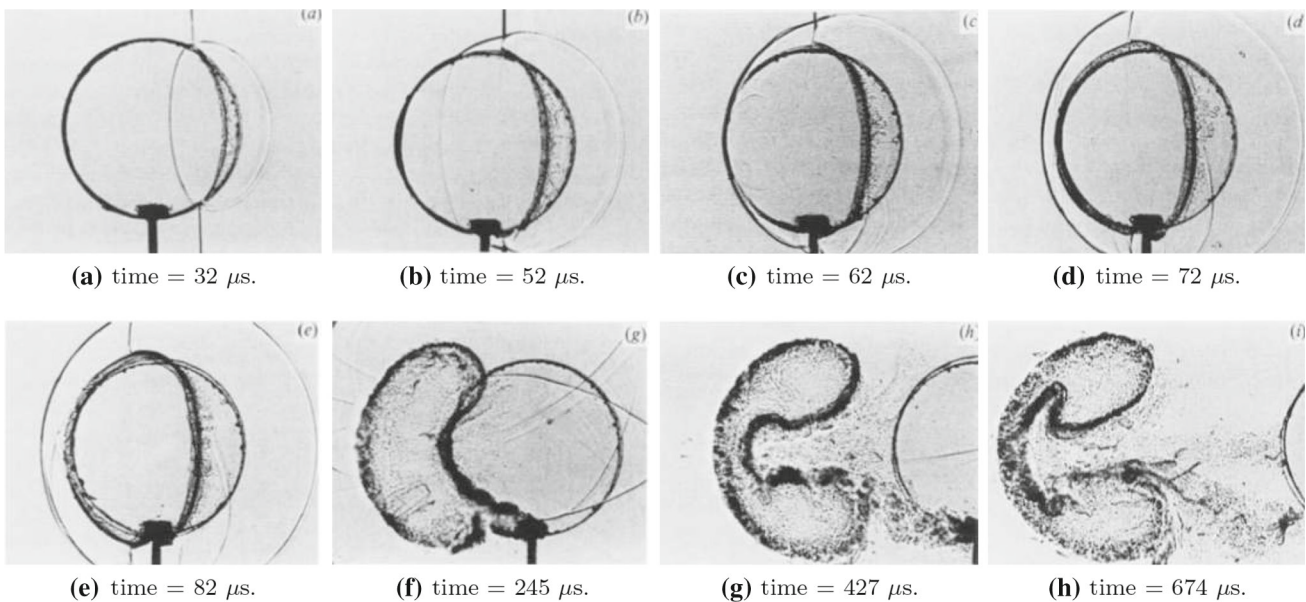
(a) time = 32 μs.   **(b)** time = 52 μs.   **(c)** time = 62 μs.   **(d)** time = 72 μs.

(e) time = 82 μs.   **(f)** time = 245 μs.   **(g)** time = 427 μs.   **(h)** time = 674 μs.

Fig. 8 Time evolution of numerical Schlieren contours for the shock–helium gas cylinder interaction problem with a $M = 1.22$ shock moving from right to left. The red dotted outline denotes the cylinder's initial location

(a) time = 32 μs.   **(b)** time = 52 μs.   **(c)** time = 62 μs.   **(d)** time = 72 μs.

(e) time = 82 μs.   **(f)** time = 245 μs.   **(g)** time = 427 μs.   **(h)** time = 674 μs.

Fig. 9 Shadow photographs of the interaction of an $M = 1.22$ shock wave moving from right to left over a cylindrical helium volume (5 cm diameter). Adapted from [47] with permission

5.4 2D shock–water/Zener solid cylinder interaction problems

We study shock–droplet/cylinder interaction problems with density ratios of 1000:1 between the material in the cylinder and the surrounding air. This problem has been studied experimentally [53] and numerically simulated with the Euler equations using FDS schemes in 3D [54] and with the AUSM schemes [10–12,55]. The shock–water cylinder interaction problem of [12] is adapted as shown in Fig. 10. The initial cylinder radius is 3.2 mm. The domain extends three

initial bubble radii in both directions: $x, y \in [-9.6\,\text{mm}, 9.6\,\text{mm}]$. The resolution is 128 points per initial cylinder radius. The shock is initialized at $x = -2\,\text{mm}$, using the Rankine–Hugoniot conditions for a $M = 1.47$ normal shock propagating from left to right. The initial cylinder radius and conservative variables are initialized in the same fashion as in Sect. 5.3. The Courant number is $\nu = 0.15$, and AUSM$^+$-up velocity–stress coupling coefficients are $k_p = k_u = 1$. Our simulations did not require the variable mixing (blending) procedure [10–12,56] where mixing is introduced to
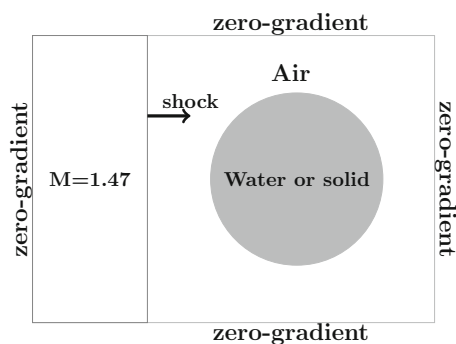
Fig. 10 Shock–cylinder interaction problem setup adapted from Chang et al. [10]

prevent the occurrence of non-physical negative pressures and improve numerical stability.

We consider two different materials for the cylinder: water and Zener material. We seek to evaluate the effect of the viscoelasticity on the wave dynamics by considering the numerical Schlieren and pressure contours and on the stress response in the time evolution of the maximum von Mises stress in the domain. Thus, the material properties of the cylinders are set such that viscoelasticity is the only difference between the two simulations. The material properties in Table 1 are used for the surrounding air and cylinder materials. For both cylinder materials, $\rho = 1000\,\text{kg/m}^3$ and $\kappa = 0.615\,\text{W/(K m)}$. By contrast to [12], which used the stiffened-gas EOS, our simulations are conducted with the NASG EOS to model the cylinder. Therefore, the speed of sound of the materials in the cylinders is higher and we expect to see small differences in numerical Schlieren and pressure contours when compared to [12]. In the water case, the compressible Navier–Stokes solutions are solved. For the Zener solid case, the model in Sect. 3.1 is solved with one relaxation time, $\mu_\text{b} = 50\,\text{mPa s}$, $G = 1\,\text{MPa}$, $G_\text{r} = 0.5\,\text{MPa}$, $\varsigma^{(1)} = 1$, and $\theta^{(1)} = 10\,\text{MHz}$. Simulation results of the numerical Schlieren function of [10,12], $(1 + (\alpha^{(1)})^2)\log(|\nabla\rho| + 1)$, and pressure are presented in Figs. 11 and 12 for the shock–water and shock–viscoelastic solid cylinder cases, respectively.

Water Due to the acoustic impedance mismatch between the water and air, the shock is partially transmitted and reflected as a shock upon interaction with the cylinder. Since water has a higher speed of sound than air, the transmitted shock propagates ahead of the shock in air and interacts with the downstream interface. The transmitted shock is partially reflected as a rarefaction and focused upstream into the cylinder (frame a and e). This process continues with phase inversion upon each reflection (frames b and f). Upon the third interaction with the downstream interface, two cusps with negative pressure are observed, similar to those in [12]. However, this feature is further evolved in the present sim-

ulations due to a faster speed of sound in the liquid when using the NASG EOS. A shock is also transmitted into the domain, although it is too weak to be visible in the contours. Numerical oscillations in both the numerical Schlieren and pressure contours along the interface are likely due to the carbuncle phenomenon and are also observed in [12]. The shock diffracted from the partial reflection and the incident shock continue to propagate and are not affected by the flow inside the cylinder. The transmitted shock propagates back to the downstream cylinder interface and is reflected to form a small hoop where a compressive wave is focused (frame c and g). At $t = 18.75\,\mu\text{s}$, the small hoop wave advects downstream and evolves into another tensile bow wave with two compressive wing-like waves (frame d and h). We conclude that despite the speed of sound differences and the minor effect of the carbuncle phenomenon [57], the results are qualitatively comparable to [12].

Zener material We set the shear modulus $G = 10\,\text{MPa}$ such that it is significant enough to illustrate the effect of viscoelasticity while maintaining a similar speed of sound relative to the water case. Thus, the pressure wave propagation is similar while the differences are attributed to the viscoelasticity. In the Schlieren images, the weak waves are attributed to the elastic shear waves that are slower than the main wave structures described in the water case. The two cusps (frames a and e), tensile wave (frames b and f), small hoop (frames c and f), and tensile wave with compressive wing-like waves (frames d and h) described in the water case are observed for the Zener solid cylinder. The elasticity increases the stress response at the top and bottom of the cylinder interface as the diffracted shock weakens. Moreover, the incident and diffracted shocks are slightly affected with diffracted elastic shear waves distorting the flow behind the diffracted shock (frames b–d). At later times, the wave structures inside the cylinder are significantly distorted due to the shear waves and weak numerical oscillations, with the latter due to the limited dissipation (frames f and g). These oscillations could be addressed by introducing numerical dissipation for the tangential components, $u_{l,i+1/2}$ and $\eta_{kk,i+1/2}$, of the generalized AUSM$^+$-up scheme in (27) and (28). However, it remains unclear how to properly introduce dissipation in the tangential direction without significantly increasing the scheme's numerical stiffness.

To observe the effect of viscoelasticity, we consider the von Mises stress as a quantity of interest

$$\sigma_\text{von} = \sqrt{(\sigma_{11})^2 - \sigma_{11}\sigma_{22} + (\sigma_{22})^2 + 3(\sigma_{12})^2}, \qquad (38)$$

which incorporates pressure and all three elastic components of the Cauchy stress tensor. The time evolution of the von Mises stress is shown in Fig. 13 for the water and Zener solid cylinders. The effect of the incident shock interacting with the
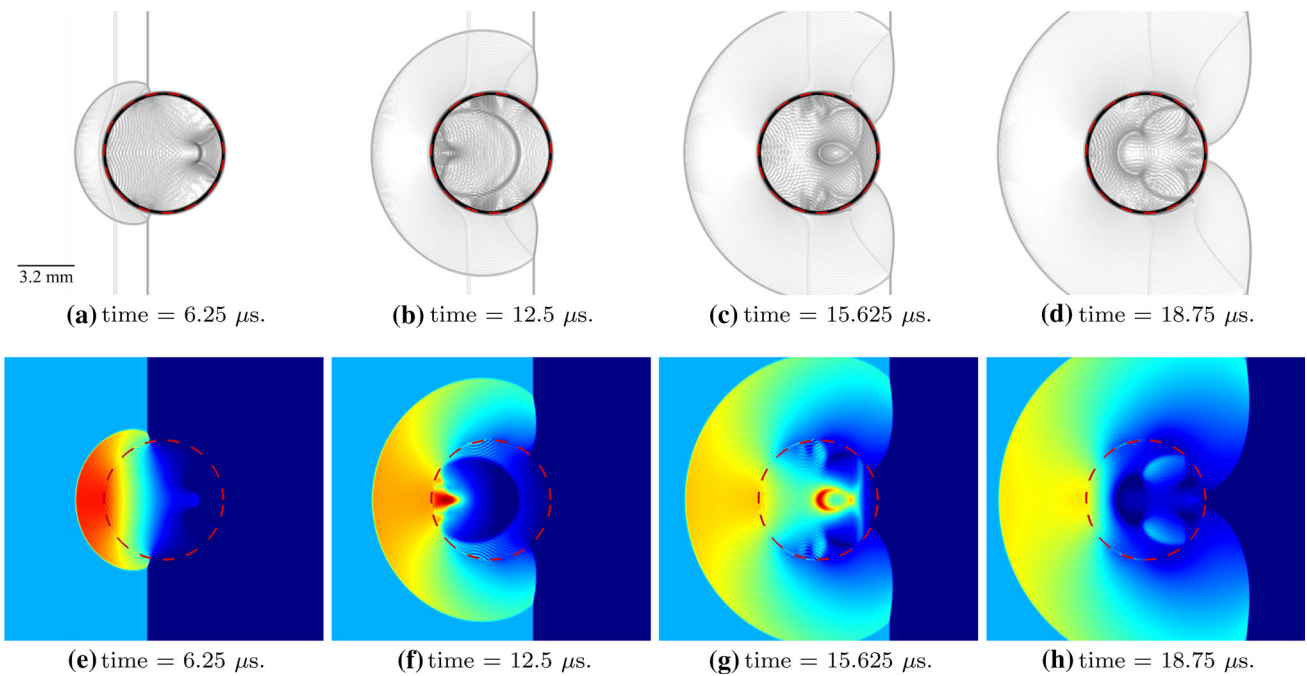
(a) time = 6.25 μs. **(b)** time = 12.5 μs. **(c)** time = 15.625 μs. **(d)** time = 18.75 μs.

(e) time = 6.25 μs. **(f)** time = 12.5 μs. **(g)** time = 15.625 μs. **(h)** time = 18.75 μs.

Fig. 11 Time evolution of numerical Schlieren (top) and pressure (bottom) contours for the shock–water cylinder interaction problem. The red dotted outline denotes the cylinder's initial location
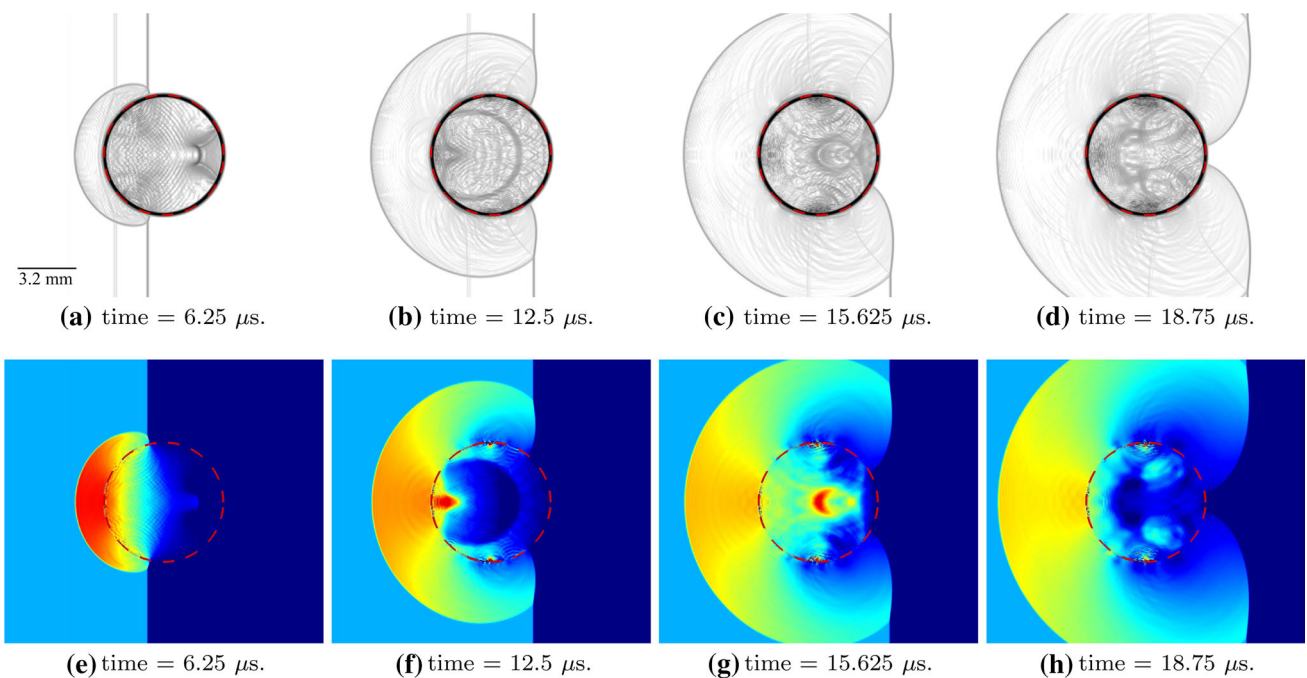

(a) time = 6.25 μs. **(b)** time = 12.5 μs. **(c)** time = 15.625 μs. **(d)** time = 18.75 μs.

(e) time = 6.25 μs. **(f)** time = 12.5 μs. **(g)** time = 15.625 μs. **(h)** time = 18.75 μs.

Fig. 12 Time evolution of numerical Schlieren (top) and pressure (bottom) contours for the shock–Zener solid cylinder interaction problem. The red dotted outline denotes the cylinder's initial location

cylinders and being partly transmitted and partly reflected is apparent in the von Mises stress profile at $t = 2\,\mu$s. Starting at $t \approx 3\,\mu$s, the profiles diverge as the von Mises stress is significantly increased in the Zener case. At times $t \approx 7\,\mu$s

and $t \approx 11\,\mu$s, the transmitted shock is reflected into the cylinder and doubles in strength. The subsequent peaks in the von Mises stress profiles are attributed to the internal shocks interacting. Moreover, the results demonstrate the capability
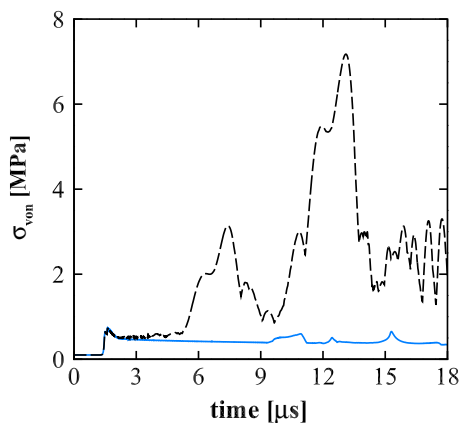
Fig. 13 Time evolution of the von Mises stress for the 2D shock–cylinder interaction problem. Blue solid line: water; black dashed line: Zener solid

of the AUSM$^+$-up extension to the five-equation multiphase model with linear viscoelasticity.

6 Conclusions

In this work, we extend the AUSM scheme to the five-equation compressible multiphase model with viscoelasticity. Stress relaxation, elasticity, and viscosity are included to describe viscoelastic media, whose deformations are assumed to be infinitesimally small such that linear viscoelasticity applies. By taking an objective Lie derivative of the constitutive relation, evolution equations are introduced for the elastic contribution of the Cauchy stress tensor, while strains are transformed into velocity gradients. We generalize AUSM schemes to account for the Cauchy stress tensor appearing in the viscoelastic description. We determine the appropriate discretization of the non-conservative volume fraction evolution equation in the five-equation multiphase model to prevent spurious oscillations at material interfaces. The resulting framework is built upon a spatial scheme that is solution adaptive and high order using explicit central differences in smooth regions and WENO primitive variable reconstruction for discontinuities. We conduct 1D numerical simulations demonstrating the approach's ability to maintain equilibrium conditions at interfaces and solve multi-material Riemann problems for gas–liquid and gas–viscoelastic solid configurations. 2D problems involving shock–cylinder problems for different fluids are computed, with density ratios up to 1000:1. Qualitative agreement is obtained with past experiments and simulations. Using our proposed approach, we successfully simulate the interaction of a shock wave interacting with a viscoelastic medium, and use the simulations to quantitatively investigate the stresses produced in the object.

References

1. Reisman, G.E., Wang, Y.C., Brennen, C.E.: Observations of shock waves in cloud cavitation. J. Fluid Mech. **355**, 255–283 (1998). https://doi.org/10.1017/S0022112097007830
2. Gnanaskandan, A., Mahesh, K.: A numerical method to simulate turbulent cavitating flows. Int. J. Multiph. Flow **70**, 22–34 (2015). https://doi.org/10.1016/j.ijmultiphaseflow.2014.11.009
3. Ganesh, H., Mäkiharju, S.A., Ceccio, S.L.: Bubbly shock propagation as a mechanism for sheet-to-cloud transition of partial cavities. J. Fluid Mech. **802**, 37–78 (2016). https://doi.org/10.1017/jfm.2016.425
4. Liou, M.S., Steffen, C.J.: A new flux splitting scheme. J. Comput. Phys. **107**, 23–39 (1993). https://doi.org/10.1006/jcph.1993.1122
5. Liou, M.S.: A sequel to AUSM, Part II: AUSM$^+$-up for all speeds. J. Comput. Phys. **214**, 137–170 (2006). https://doi.org/10.1016/j.jcp.2005.09.020
6. Shima, E., Kitamura, K.: Parameter-free simple low-dissipation AUSM-family scheme for all speeds. AIAA J. **49**, 1693–1709 (2011). https://doi.org/10.2514/1.J050905
7. Paillère, H., Corre, C., García Cascales, J.R.: On the extension of the AUSM$^+$ scheme to compressible two-fluid models. Comput. Fluids **32**, 891–916 (2003). https://doi.org/10.1016/S0045-7930(02)00021-X
8. Evje, S., Fjelde, K.K.: On a rough AUSM scheme for a one-dimensional two-phase model. Comput. Fluids **32**, 1497–1530 (2003). https://doi.org/10.1016/S0045-7930(02)00113-5
9. Chang, C.H., Liou, M.S.: A new approach to the simulation of compressible multifluid flows with AUSM$^+$ scheme. 16th AIAA Computational Fluid Dynamics Conference, Orlando, FL, AIAA Paper 2003-4107 (2003). https://doi.org/10.2514/6.2003-4107
10. Chang, C.H., Liou, M.S.: A robust and accurate approach to computing compressible multiphase flow: Stratified flow model and AUSM$^+$-up scheme. J. Comput. Phys. **225**, 840–873 (2007). https://doi.org/10.1016/j.jcp.2007.01.007
11. Liou, M.S., Chang, C.H., Nguyen, L., Theofanous, T.G.: How to solve compressible multifluid equations: A simple, robust, and accurate method. AIAA J. **46**, 2345–2356 (2008). https://doi.org/10.2514/1.34793
12. Kitamura, K., Liou, M.S., Chang, C.H.: Extension and comparative study of AUSM-family schemes for compressible multiphase flow simulations. Commun. Comput. Phys. **16**, 632–674 (2014). https://doi.org/10.4208/cicp.020813.190214a
13. Gavrilyuk, S.L., Favrie, N., Saurel, R.: Modelling wave dynamics of compressible elastic materials. J. Comput. Phys. **227**, 2941–2969 (2008). https://doi.org/10.1016/j.jcp.2007.11.030
14. Barton, P.T., Obadia, B., Drikakis, D.: A conservative level-set based method for compressible solid/fluid problems on fixed grids. J. Comput. Phys. **230**, 7867–7890 (2011). https://doi.org/10.1016/j.jcp.2011.07.008
15. Barton, P.T., Deiterding, R., Meiron, D., Pullin, D.: Eulerian adaptive finite-difference method for high-velocity impact and penetration problems. J. Comput. Phys. **240**, 76–99 (2013). https://doi.org/10.1016/j.jcp.2013.01.013

16. López Ortega, A., Lombardini, M., Barton, P., Pullin, D., Meiron, D.: Richtmyer Meshkov instability for elasticplastic solids in converging geometries. J. Mech. Phys. Solids **76**, 291–324 (2015). https://doi.org/10.1016/j.jmps.2014.12.002

17. Ndanou, S., Favrie, N., Gavrilyuk, S.: Multi-solid and multi-fluid diffuse interface model: applications to dynamic fracture and fragmentation. J. Comput. Phys. **295**, 523–555 (2015). https://doi.org/10.1016/j.jcp.2015.04.024

18. Rodriguez, M., Johnsen, E.: A high-order accurate five-equations compressible multiphase approach for viscoelastic fluids and solids with relaxation and elasticity. J. Comput. Phys. **379**, 70–90 (2019). https://doi.org/10.1016/j.jcp.2018.10.035

19. Eringen, A.C.: Nonlinear Theory of Continuous Media. McGraw-Hill, New York (1962)

20. Luo, H., Baum, J.D., Löhner, R.: On the computation of multi-material flows using ALE formulation. J. Comput. Phys. **194**, 304–328 (2004). https://doi.org/10.1016/j.jcp.2003.09.026

21. McGurn, M.T., Ruggirello, K.P., DesJardin, P.E.: An Eulerian-Lagrangian moving immersed interface method for simulating burning solids. J. Comput. Phys. **241**, 364–387 (2013). https://doi.org/10.1016/j.jcp.2013.01.045

22. Alahyari Beig, S., Johnsen, E.: Maintaining interface equilibrium conditions in compressible multiphase flows using interface capturing. J. Comput. Phys. **302**, 548–566 (2015). https://doi.org/10.1016/j.jcp.2015.09.018

23. He, Z., Zhang, Y., Li, X., Tian, B.: Preventing numerical oscillations in the flux-split based finite difference method for compressible flows with discontinuities. Int. J. Numer. Methods Fluids **80**, 306–316 (2016). https://doi.org/10.1002/fld.4080

24. Saurel, R., Abgrall, R.: A simple method for compressible multifluid flows. SIAM J. Sci. Comput. **21**, 1115–1145 (1999). https://doi.org/10.1137/S1064827597323749

25. Johnsen, E., Colonius, T.: Implementation of WENO schemes in compressible multicomponent flow problems. J. Comput. Phys. **219**, 715–732 (2006). https://doi.org/10.1016/j.jcp.2006.04.018

26. Scandaliato, A.L., Liou, M.S.: AUSM-based high-order solution for Euler equations. Commun. Comput. Phys. **12**, 1096–1120 (2012). https://doi.org/10.4208/cicp.250311.081211a

27. Le Métayer, O., Saurel, R.: The Noble-Abel Stiffened-Gas equation of state. Phys. Fluids **28**, 046102 (2016). https://doi.org/10.1063/1.4945981

28. Harlow, F.H., Amsden, A.A.: Fluid Dynamics. Los Alamos Scientific Laboratory, Los Alamos (1971)

29. Le Métayer, O., Massoni, J., Saurel, R.: Modelling evaporation fronts with reactive Riemann solvers. J. Comput. Phys. **205**, 567–610 (2005). https://doi.org/10.1016/j.jcp.2004.11.021

30. Zener, C.: Mechanical behavior of high damping metals. J. Appl. Phys. **18**, 1022–1025 (1947). https://doi.org/10.1063/1.1697572

31. Carcione, J.M.: Wave Fields in Real Media. Wave Propagation in Anisotropic, Anelastic, Porous and Electromagnetic Media, 3rd edn. Elsevier, Amsterdam (2014). https://doi.org/10.1016/C2013-0-18893-9

32. Fung, Y.C.: Biomechanics. Springer, New York (1993). https://doi.org/10.1007/978-1-4757-2257-4

33. Wineman, A.S.: Mechanical Response of Polymers: An Introduction. Cambridge University Press, Cambridge (2000)

34. Altmeyer, G., Rouhaud, E., Panicaud, B., Roos, A., Kerner, R., Wang, M.: Viscoelastic models with consistent hypoelasticity for fluids undergoing finite deformations. Mech. Time-Depend. Mater. **19**, 375–395 (2015). https://doi.org/10.1007/s11043-015-9269-5

35. Lombard, B., Piraux, J.: Numerical modeling of transient two-dimensional viscoelastic waves. J. Comput. Phys. **230**, 6099–6114 (2011). https://doi.org/10.1016/j.jcp.2011.04.015

36. Allaire, G., Clerc, S., Kokh, S.: A five-equation model for the simulation of interfaces between compressible fluids. J. Comput. Phys. **181**, 577–616 (2002). https://doi.org/10.1006/jcph.2002.7143

37. Murrone, A., Guillard, H.: A five equation reduced model for compressible two phase flow problems. J. Comput. Phys. **202**, 664–698 (2005). https://doi.org/10.1016/j.jcp.2004.07.019

38. Perigaud, G., Saurel, R.: A compressible flow model with capillary effects. J. Comput. Phys. **209**, 139–178 (2005). https://doi.org/10.1016/j.jcp.2005.03.018

39. Shukla, R.K., Pantano, C., Freund, J.B.: An interface capturing method for the simulation of multi-phase compressible flows. J. Comput. Phys. **229**, 7411–7439 (2010). https://doi.org/10.1016/j.jcp.2010.06.025

40. Henry de Frahan, M.T., Varadan, S., Johnsen, E.: A new limiting procedure for discontinuous Galerkin methods applied to compressible multiphase flows with shocks and interfaces. J. Comput. Phys. **280**, 489–509 (2015). https://doi.org/10.1016/j.jcp.2014.09.030

41. Liou, M.S.: A sequel to AUSM: AUSM$^+$. J. Comput. Phys. **129**, 364–382 (1996). https://doi.org/10.1006/jcph.1996.0256

42. Liou, M.S.: On a new class of flux splittings. In: Napolitano, M., Sabetta, F. (eds.) Thirteenth International Conference on Numerical Methods in Fluid Dynamics: Proceedings of the Conference Held at the Consiglio Nazionale delle Ricerche Rome, Italy. Lecture Notes in Physics, vol. 414, pp. 115–119. Springer, Berlin (1992). https://doi.org/10.1007/3-540-56394-6_199

43. Abgrall, R.: How to prevent pressure oscillations in multicomponent flow calculations: a quasi conservative approach. J. Comput. Phys. **125**, 150–160 (1996). https://doi.org/10.1006/jcph.1996.0085

44. Shyue, K.M.: An efficient shock-capturing algorithm for compressible multicomponent problems. J. Comput. Phys. **142**, 208–242 (1998). https://doi.org/10.1006/jcph.1998.5930

45. Johnsen, E.: On the treatment of contact discontinuities using WENO schemes. J. Comput. Phys. **230**, 8665–8668 (2011). https://doi.org/10.1016/j.jcp.2011.08.017

46. Fedkiw, R.P., Marquina, A., Merriman, B.: An isobaric fix for the overheating problem in multimaterial compressible flows. J. Comput. Phys. **148**, 545–578 (1999). https://doi.org/10.1006/jcph.1998.6129

47. Haas, J.F., Sturtevant, B.: Interaction of weak shock waves with cylindrical and spherical gas inhomogeneities. J. Fluid Mech. **181**, 41–76 (1987). https://doi.org/10.1017/S0022112087002003

48. Quirk, J.J., Karni, S.: On the dynamics of a shock–bubble interaction. J. Fluid Mech. **318**, 129–163 (1996). https://doi.org/10.1017/S0022112096007069

49. Fedkiw, R.P., Aslam, T., Merriman, B., Osher, S.: A non-oscillatory Eulerian approach to interfaces in multimaterial flows (the Ghost Fluid Method). J. Comput. Phys. **152**, 457–492 (1999). https://doi.org/10.1006/jcph.1999.6236

50. Don, W.S., Quillen, C.B.: Numerical simulation of shock-cylinder interactions: I. Resolution. J. Comput. Phys. **122**, 244–265 (1995). https://doi.org/10.1006/jcph.1995.1211

51. Wang, L., Currao, G.M., Han, F., Neely, A.J., Young, J., Tian, F.B.: An immersed boundary method for fluidstructure interaction with compressible multiphase flows. J. Comput. Phys. **346**, 131–151 (2017). https://doi.org/10.1016/j.jcp.2017.06.008

52. Henderson, L.F., Colella, P., Puckett, E.G.: On the refraction of shock waves at a slow–fast gas interface. J. Fluid Mech. **224**, 1–27 (1991). https://doi.org/10.1017/S0022112091001623

53. Theofanous, T.G., Li, G.J., Dinh, T.N.: Aerobreakup in rarefied supersonic gas flows. J. Fluids Eng. **126**, 516–527 (2004). https://doi.org/10.1115/1.1777234

54. Meng, J.C., Colonius, T.: Numerical simulation of the aerobreakup of a water droplet. J. Fluid Mech. **835**, 1108–1135 (2018). https://doi.org/10.1017/jfm.2017.804

55. Niu, Y.Y., Lin, Y.C., Chang, C.H.: A further work on multi-phase two-fluid approach for compressible multi-phase flows. Int. J.

Numer. Methods Fluids **58**, 879–896 (2008). https://doi.org/10.1002/fld.1773

56. Pandare, A.K., Luo, H.: A robust and efficient finite volume method for compressible inviscid and viscous two-phase flows. J. Comput. Phys. **371**, 67–91 (2018). https://doi.org/10.1016/j.jcp.2018.05.018

57. Pandolfi, M., D'Ambrosio, D.: Numerical instabilities in upwind methods: Analysis and cures for the "Carbuncle" phenomenon. J. Comput. Phys. **166**, 271–301 (2001). https://doi.org/10.1006/jcph.2000.6652